THE GEOLOGICAL SOCIETY OF AMERICA®

How a strong low-angle normal fault formed: The Whipple detachment, southeastern California

Gary J. Axen†
Department of Earth and Environmental Science, New Mexico Institute of Mining and Technology, Socorro, New Mexico 87801, USA

ABSTRACT

Many low-angle normal faults (dip ≤30°) accommodate tens of kilometers of crustal extension, but their mechanics remain contentious. Most models for low-angle normal fault slip assume vertical maximum principal stress σ_1, leading many authors to conclude that low-angle normal faults are poorly oriented in the stress field (≥60° from σ_1) and weak (low friction). In contrast, models for low-angle normal fault formation in isotropic rocks typically assume Coulomb failure and require inclined σ_1 (no misorientation). Here, a data-based, mechanical-tectonic model is presented for formation of the Whipple detachment fault, southeastern California. The model honors local and regional geologic and tectonic history and laboratory friction measurements. The Whipple detachment fault formed progressively in the brittle-plastic transition by linking of "minidetachments," which are small-scale analogs (meters to kilometers in length) in the upper footwall.

Minidetachments followed mylonitic anisotropy along planes of maximum shear stress (45° from the maximum principal stress), not Coulomb fractures. They evolved from mylonitic flow to cataclasis and frictional slip at 300–400 °C and ~9.5 km depth, while fluid pressure fell from lithostatic to hydrostatic levels. Minidetachment friction was presumably high (0.6–0.85), based upon formation of quartzofeldspathic cataclasite and pseudotachylyte. Similar mechanics are inferred for both the minidetachments and the Whipple detachment fault, driven by high differential stress (~150–160 MPa). A Mohr construction is presented with the fault dip as the main free parameter. Using "Byerlee friction" (0.6–0.85) on the minidetachments and the Whipple detachment fault, and internal friction (1.0–1.7) on newly formed Reidel shears, the initial fault dips are calculated at 16°–26°, with σ_1 plunging ~61°–71° northeast. Linked minidetachments probably were not well aligned, and slip on the evolving Whipple detachment fault probably contributed to fault smoothing, by off-fault fracturing and cataclasis, and to formation of the fault core and fractured damage zone.

Stress rotation may have occurred only within the mylonitic shear zone, but asymmetric tectonic forces applied to the brittle crust probably caused gradual rotation of σ_1 above it as a result of: (1) the upward force applied to the base of marginal North America by buoyant asthenosphere upwelling into an opening slab-free window and/or (2) basal, top-to-the-NE shear traction due to midcrustal mylonitic flow during tectonic exhumation of the Orocopia Schist. The mechanical-tectonic model probably applies directly to low-angle normal faults of the lower Colorado River extensional corridor, and aspects of the model (e.g., significance of anisotropy, stress rotation) likely apply to formation of other strong low-angle normal faults.

INTRODUCTION

Earthquake hazard assessment and natural resource exploration depend on understanding fault evolution and mechanics, yet even the shear strength of most faults is uncertain (Faulkner et al., 2010). Low-angle normal faults were well documented by the 1980s (Crittenden et al., 1980; Wernicke, 1981; Wernicke and Burchfiel, 1982) and are found in diverse continental settings (e.g., Wernicke, 1995; Burchfiel et al., 1992; Lister et al., 1984; Whitney and Dilek, 1997; Axen, 2004; Collettini et al., 2006; Reston, 2009; Collettini, 2011; Whitney et al., 2013; Little et al., 2019) and mid-ocean ridges (Karson et al., 2006). Nevertheless, the mechanics of low-angle normal fault formation and slip remain enigmatic (Axen, 2004; Collettini, 2011).

On many continental low-angle normal faults, large-magnitude slip exhumed plutonic-metamorphic footwalls from below the strong, midcrustal brittle-plastic transition (e.g., Fig. 1A), forming metamorphic core complexes. In these structures, shear- and fault-zone rocks form progressively during footwall exhumation, and crystal-plastic mylonites are overprinted by frictional-cataclastic textures (e.g., Davis et al., 1986; Davis, 1988). Removal and dramatic thinning of upper plates drive isostatic footwall rebound, which induces lower- or mid-crustal flow, arching low-angle normal faults and their footwalls (Fig. 1C), and back-tilting parts of both (Spencer, 1984; Wernicke and Axen, 1988; Buck, 1988).

Mechanical understanding of low-angle normal fault slip typically is hindered by incomplete data, and the vertical maximum principal stress, σ_1, is commonly assumed (Anderson 1942; Sibson, 1985; Axen and Selverstone, 1994; Collettini and Sibson, 2001), leading to suggestions that low-angle normal faults are poorly oriented for slip and therefore weak (Axen, 2004; Collettini, 2011). Weakness may arise from low-friction fault-zone materials (e.g., Hayman, 2006; Haines and van der Pluijm, 2012), evaporites (Yuan et al., 2017), and/or elevated pore-fluid pressure, P_f, causing low effective normal stress (Smith et al., 2008). However, several strong low-angle normal faults (Collettini, 2011), including the Whipple detachment fault, lack evidence for high P_f or weak fault rocks.

Low-angle normal faults are mechanically more difficult to form than to slip once formed. Static elastic models (Fig. 2) of isotropic crust require nonvertical σ_1 to predict Coulomb low-angle normal fault trajectories. In these, asymmetric boundary conditions cause stress rotation: lateral gradients of basal normal traction (Spencer and Chase, 1989) or basal shear traction (Yin, 1989). Deep viscous flow may apply shear to the base of the brittle crust (Lister and Davis, 1989; Westaway, 1999), but it presents a chicken-and-egg problem, because lower-crustal flow is commonly considered to be a response to isostatic unloading due to low-angle normal fault slip (Block and Royden, 1990; Wdowinski and Axen, 1992; Lavier et al., 1999; Whitney et al., 2013). Mechanical anisotropy, also

†gary.axen@nmt.edu.

GSA Bulletin; https://doi.org/10.1130/B35386.1; 7 figures; 1 table.

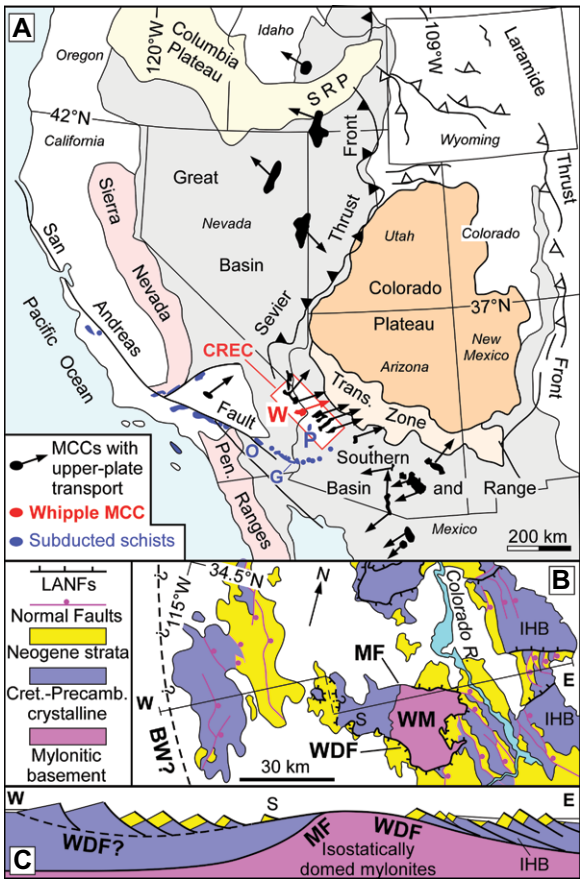

Figure 1. (A) Tectonic setting of several North American metamorphic core complexes (MCCs; black, with arrows showing upper-plate transport; Whipple footwall [W] shown in red) and the lower Colorado River extensional corridor (CREC) adjacent to the Colorado Plateau–Basin and Range transition (Trans.) zone. Orocopia and related schists are blue (O—Orocopia Mountains, G—Gavilan Hills, P—Plomosa Mountains). Pen. Ranges—Peninsular Ranges. (B) Simplified tectonic map of the Whipple Mountains (WM) area, showing the Whipple detachment fault (WDF), mylonite front (MF), and possible detachment breakaway (BW?). Savahia Peak (S) is the westernmost certain Whipple detachment fault exposure. Wide, strongly tilted, intact hanging-wall blocks (IHB) restore west of the mylonite front. LANFs—low-angle normal faults. (C) Schematic cross section along the line shown in B. Data for part A are from Wust (1986), Spencer and Reynolds (1989), Chapman (2017), Axen et al. (2018), and Strickland et al. (2018). B and C are modified from Howard and John (1987).

appealed to here, controls primary low dips of some low-angle normal faults (Miller et al., 1983; Axen, 1993), but others cut across stratigraphy and preexisting structure (e.g., Wernicke et al., 1985; Axen et al., 1990). Some numerical models reproduce cross-sectional geometries of continental low-angle normal faults through isostatic tilting of initially steep faults (>45°) that lock up once they become gently dipping (Buck, 1988; Lavier et al., 1999; Choi et al., 2013). Such models may apply to oceanic low-angle normal faults (Garcés and Gee, 2007), but they conflict with the primary low dips of many continental low-angle normal faults (Wernicke, 1995; Axen and Bartley, 1997; Axen, 2004; Collettini, 2011).

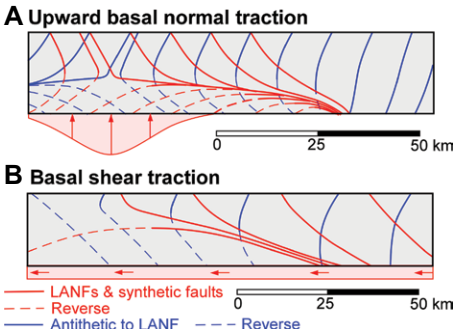

Figure 2. Static elastic models with asymmetric boundary conditions that cause stress trajectories consistent with Coulomb failure of low-angle normal faults (LANFs). Blue and red lines show predicted conjugate fault trajectories, solid for normal faults and dashed for reverse. (A) Upward buoyant force flexes the elastic crust (Spencer and Chase, 1989). (B) Basal shear traction (Yin, 1989).

In this paper, I present a compelling, data-based, mechanical model for progressive formation of the Whipple detachment fault in the brittle-plastic transition (the zone of maximum crustal strength where brittle processes give way downward to penetrative flow; e.g., Brace and Kohlstedt, 1980). The evolution of "minidetachments," which are meter- to kilometer-scale analogs of the main detachment, guides the conceptual model. In summary, initial frictional-cataclastic slip on minidetachments occurs in the brittle-plastic transition, on mylonitic C planes oriented ~45° to σ_1. Many preserved C planes display aligned chlorite, so their friction was probably low. I infer that minidetachments become linked episodically, progressively forming the main detachment fault, which propagates upward at low dip, maintained by isostatic footwall rebound and lengthening as footwall exhumation proceeds. Pore-fluid pressure drops from lithostatic to hydrostatic as random-fabric quartzofeldspathic cataclasites form, increasing friction to 0.6–0.85. The regional tectonic evolution around the Whipple detachment fault suggests plausible causes of stress rotation above the mylonite zone.

WHIPPLE DETACHMENT FAULT

The Whipple detachment fault (Figs. 1 and 3) is one of several coeval, kinematically coordinated, low-angle normal faults that formed the metamorphic core complexes of the lower Colorado River extensional corridor. Approximately 50 km of top-to-the-NE normal-sense shear exhumed Colorado River extensional corridor footwalls through the brittle-plastic transition (Howard and John, 1987; Davis, 1988; Singleton et al., 2014). Most share aspects of the Whipple detachment fault evolution. Post-detachment deformation in the Colorado River extensional corridor is minor (Howard and John, 1987; Spencer and Reynolds, 1991). Restoration of low-angle normal fault slip places Colorado River extensional corridor footwalls beneath the Colorado Plateau–Basin and Range transition zone (Fig. 1A).

The eastern Whipple detachment fault footwall displays a domed, retrograde (amphibolite- to greenschist-facies) mylonite shear zone ≥1 km thick (base not exposed), in which mainly top-to-the-NE simple shear overprinted Proterozoic orthogneiss and Mesozoic plutons (Davis, 1988; Davis and Lister, 1988; Behr and Platt, 2011). Brittle deformation overprints the upper mylonites (Figs. 3A–3C; Davis, 1988; Davis and Lister, 1988; Luther et al., 2013). The "chlorite breccia zone" includes ~100 m of a chlorite + epidote–altered, fractured damage zone overlain by ~10 m of similarly altered cataclasite of the outer fault core. In turn, this is overlain and overprinted by the "microbreccia ledge," represented by ~0.2–2 m of resistant ultracataclasite (inner fault core) that is capped by the sharp, NE-SW–striated principal slip surface.

The mylonite front (Figs. 1B and 1C) separates structurally higher, mainly nonmylonitic western footwall from the structurally deeper, mostly mylonitic eastern footwall, and it is generally interpreted as the west-tilted top of a fossil brittle-plastic transition (Davis, 1988; see also Singleton and Mosher, 2012). Footwall rocks west of the mylonite front are Proterozoic orthogneiss, Mesozoic plutons, and Miocene dikes. Thin, discontinuous mylonite bands cut

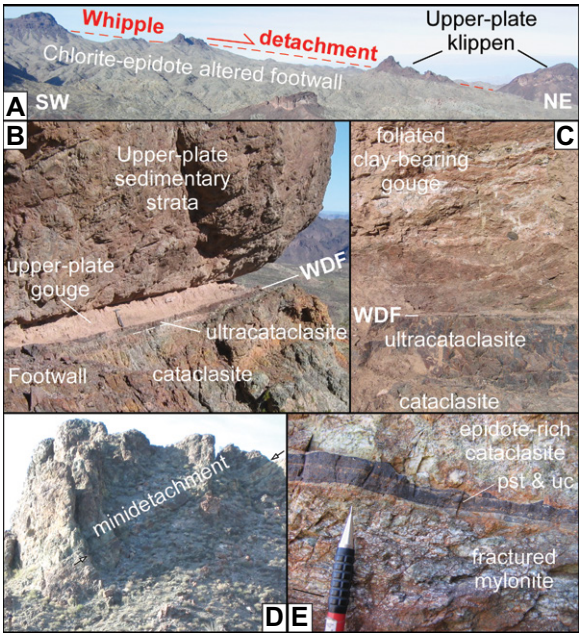

Figure 3. Photographs of the Whipple detachment fault (WDF) and minidetachments. (A) View to northwest (perpendicular to transport) in northeastern Whipple Mountains. Width of view is ~4 km. (B) Exposure of Whipple detachment fault above Bowmans Wash showing structural sequence. Hammer for scale. (C) Detail view of foliated upper-plate gouge and top of footwall. Coin for scale. (D) Minidetachment in Bowmans Wash (arrows). Person in lower left for scale. (E) Detail of same minidetachment, showing epidote-rich upper-plate cataclasite, pseudotachylyte (pst), and ultracataclasite (uc), and fractured mylonite of footwall. Thin line left of pencil shows mylonitic foliation.

these rocks up to ~1 km above the front (Davis, 1988). Western basement rocks are overlain in fault contact or nonconformably by thin sequences of Neogene volcanic and sedimentary strata (Carr et al., 1980; Davis, 1988; Yin and Dunn, 1992; Gans and Gentry, 2016). Isostatic footwall rebound tilted the mylonite front southwest (Spencer, 1984). West of the range, subhorizontal seismic reflectors below ~10 km depth are interpreted as untilted mylonites (Davis, 1988; Wang et al., 1989).

Mylonites near the front formed in conditions of ~500–300 °C and 480–290 MPa (Behr and Platt, 2011). Maximum pressure-temperature (*P-T*) estimates are consistent with those from mylonitic rocks farther east (Anderson et al., 1988). High mylonitic temperatures near the front may reflect heating by abundant Miocene dikes (see below), but the higher pressures suggest instead that early mylonitization near the front occurred at ~18 km depth. Final mylonitization there predated undeformed plutons that intruded at ca. 220 MPa (~8.5 km depth; Anderson et al., 1988; Anderson, 1996).

NW-striking dikes in the Chambers Well dike swarm (ca. 24–18 Ma) intruded the footwall along and west of the mylonite front, locally comprising up to ~60% of the volume (Davis, 1988; Gans and Gentry, 2016). Early dikes (ca. 24–20 Ma) predated final mylonitization; younger dikes and a pluton crosscut mylonites at ca. 19 Ma (Davis, 1988; Gans and Gentry, 2016). The oldest top-to-the-NE mylonites may be only a few million years older than the brittle Whipple detachment fault (Lister and Davis, 1989; Behr and Platt, 2011). The Whipple detachment fault and other Colorado River extensional corridor footwalls record rapid exhumation-related cooling from ~350 °C to <100 °C between 22–21 and ca. 13–11 Ma (Foster and John, 1999; Singleton et al., 2014, and references therein).

The western limit of extension (Figs. 1B and 1C) may mark the Whipple detachment fault breakaway (Howard and John, 1987). The present angle between the Whipple detachment fault and the mylonite front is ~15°–30° (Davis, 1988; Lister and Davis, 1989; Behr and Platt, 2011), and this may reflect initial Whipple detachment fault dip there, when mylonites were subhorizontal. The Whipple detachment fault probably had low dip for ~10 km west of the mylonite front, as far as Savahia Peak, an upper-plate klippe (Figs. 1B and 1C). The initial fault trajectory west of Savahia Peak (Fig. 1) is uncertain and may have been either gentle (Davis, 1988; Davis and Lister, 1988; Yin and Dunn, 1992) or steep (Behr and Platt, 2011; Gans and Gentry, 2016). East of the mylonite front, the Whipple detachment fault cuts gently down across mylonites that show little or no increase of metamorphic grade (Anderson et al., 1988; Behr and Platt, 2011), consistent with initially subhorizontal to gently northeast-dipping mylonites and a gentle, northeast fault dip.

Upper-plate rocks are similar to the western footwall: mainly Proterozoic gneiss overlain nonconformably by Neogene sedimentary and volcanic strata. Both are highly extended by normal faults (Howard and John, 1987; Davis, 1988; Davis and Lister, 1988). Strongly tilted, but internally little-faulted, 10+-km-wide panels of upper-plate rocks east and northeast of the Whipple Mountains restore west of the mylonite front, requiring 40+ km of Whipple detachment fault slip and initial footwall paleodepth there of 10+ km (Howard and John, 1987). The basal upper plate, where exposed, shows centimeters of clay-bearing gouge (Figs. 3B and 3C) apparently derived from overlying Neogene strata; clays are sparse in cataclasites below the Whipple detachment fault (Luther et al., 2013).

WHIPPLE DETACHMENT FAULT FORMATION AND MECHANICS

In this section, I develop a mechanical model for progressive formation of the Whipple detachment fault in the brittle-plastic transition. The model applies to the Whipple detachment fault east of the mylonite front, and mechanical aspects are based upon a well-constrained Mohr-circle construction representing the two-dimensional stress tensor during minidetachment and Whipple detachment fault formation, in a vertical, NE-SW plane parallel to the main fault transport direction. The model applies in the zone of formation in the brittle-plastic transition (Fig. 4C), beginning shortly after onset of rapid extension, when isotherm advection had reached pseudo–steady state, and until progressive Whipple detachment fault formation ended.

Evolution of Minidetachments and the Whipple Detachment Fault

"Minidetachments" (Figs. 3D and 3E; Axen and Selverstone, 1994) are meter- to kilometer-scale Whipple detachment fault analogs preserved in the upper parts of the mylonitic footwall (they have not been recognized west of the mylonite front). They record the P, T, P_f, and maximum principal stress orientation within the upper footwall as it passed through the brittle-plastic transition (Selverstone et al., 2012). Minidetachments are subparallel to the Whipple detachment fault and evolved from mylonitic shear (C) planes to sharp slip surfaces commonly overlain by random-fabric quartzofeldspathic cataclasites (Selverstone et al., 2012). Each had one to several slip events before being abandoned, and they formed when strong, retrograde epidote crystallized, impeding mylonitic flow (Selverstone et al., 2012). Most minidetachments lack connection to the Whipple detachment fault, so they are probably not splays.

Metamorphic phase equilibria and fluid inclusion analyses have shown that final mylonitization and initial frictional-cataclastic minidetachment slip both occurred at 380–420 °C and ~9.5 km depth (Fig. 4A; Selverstone et al., 2012), suggesting geologically instantaneous embrittlement. Upon embrittlement, P_f dropped

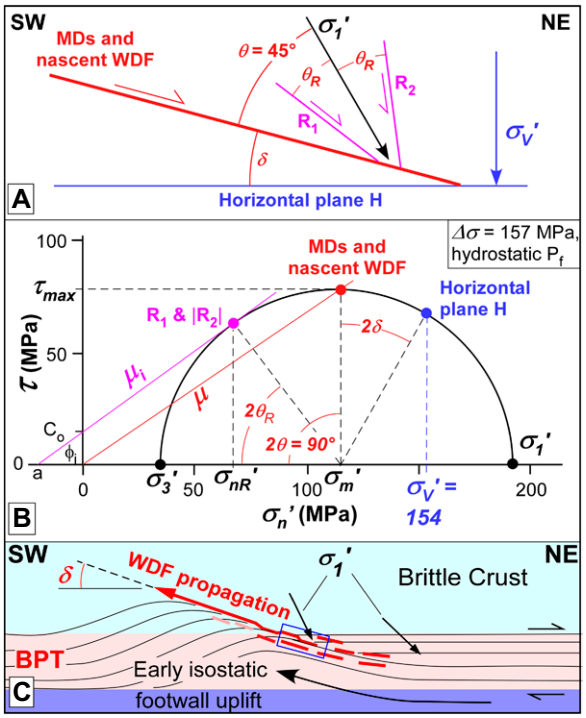

Figure 4. (A) Geometry of minidetachments (MDs) and the Whipple detachment fault (WDF) during formation in the brittle-plastic transition. The angle between primary (synthetic) R_1 and secondary (antithetic) R_2 Reidel shears, $2\theta_R$, is bisected by the effective maximum principal stress, σ_1'. The Whipple detachment fault is at angle $\theta = 45°$ to σ_1', and Whipple detachment fault dip is δ. Effective vertical normal stress σ_v' acts on horizontal plane *H*. (B) Mohr diagram for mechanics of Whipple detachment fault formation, corresponding to geometry in A (with absolute value of R_2 shear stress). C_0 is cohesion of R_2 shears, with internal friction μ_i corresponding to the angle of internal friction ϕ_i; μ is static friction on the Whipple detachment fault and minidetachments; P_f is pore-fluid pressure. Effective normal stress on the Whipple detachment fault and minidetachments equals the effective mean stress σ_m'. See text for notation. (C) Evolution of Whipple detachment fault by linking of active minidetachments (short red lines; pink where abandoned) as footwall mylonites (thin black lines) exit the brittle-plastic transition (BPT). The mechanical model applies in the zone of pseudo–steady-state formation of the Whipple detachment fault (blue box).

from 290–270 MPa (late mylonitization) to 130–80 MPa (cataclasis), consistent with lithostatic and hydrostatic P_f, respectively, at ~9.5 km depth (Selverstone et al., 2012). Weak minerals and aligned mineral grains are sparse or absent in these random-fabric, quartzofeldspathic cataclasites, suggesting friction of 0.6–0.85 (e.g., Byerlee, 1978; Beeler et al., 1996; Karner et al., 1997). This is confirmed qualitatively by the pseudotachylyte (quenched frictional melt) on the minidetachments (Selverstone et al., 2012; Ortega-Arroyo et al., 2017), which requires seismogenic slip rates and high shear traction (Tsutsumi and Shimamoto, 1997), consistent with hydrostatic P_f and normal rock friction.

Synchronously, primary Reidel R_1 slip surfaces formed, either from or subparallel to mylonitic C′ shear planes, and secondary R_2 shears crosscut intact mylonitic foliation (Selverstone et al., 2012). Treating R_1 and R_2 shears as conjugate faults bisected by σ_1 (Fig. 4A; Mandl et al., 1977; Logan et al., 1992; Selverstone et al., 2012) confirms the inference that minidetachments formed at $\theta \approx 45°$ to σ_1 (Fig. 4A). This stress orientation is expected during both mylonitic flow and granular cataclastic flow (e.g., Coulomb plasticity; Marone, 1995), and it requires that maximum ambient shear traction τ_{max} acted on mylonitic C planes, on the minidetachments, and, as argued below, on the nascent Whipple detachment fault (Fig. 4B; Selverstone et al., 2012).

I infer that the Whipple detachment fault east of the mylonite front formed by episodic, progressive linking of minidetachments (Fig. 4C). Faults commonly form and grow by linkage of preexisting structures: Millimeter-scale tensile cracks link to form centimeter-scale faults in experiments (e.g., Lockner et al., 1991), preexisting joints link to form outcrop-scale strike-slip faults (e.g., Martel and Pollard, 1989), and kilometer-scale normal faults link to form basin-scale rift-bounding faults (e.g., Gawthorpe and Leeder, 2000). In all these examples, some early, small structures are abandoned and preserved without linking, explaining the preserved minidetachments. Solidification of minidetachment pseudotachylyte (e.g., Mitchell et al., 2016; Proctor and Lockner, 2016; Griffith, 2016) and increasing friction upon embrittlement (see above) likely strengthened the minidetachments, favoring abandonment and preservation. Accumulating slip and off-fault damage (fracturing, cataclasis) smoothed fault steps where misaligned structures linked (Martel and Pollard, 1989; Faulkner et al., 2010). These processes likely contributed to the damage zone and cataclastic fault core and may also have modified the frictional strength of the (presently) very smooth Whipple detachment fault.

From its zone of formation in the brittle-plastic transition, the Whipple detachment fault probably propagated up into the brittle crust at low dip, maintained by footwall uplift (Fig. 4C), regardless of initial geometries of the detachment and related faults farther west. This is supported by syntectonic upper-plate strata that record exhumation of nonmylonitic footwall rocks and abandonment of the southwestern, backtilted Whipple detachment fault, followed by exhumation of mylonites while basin formation and Whipple detachment fault slip continued northeast of the rising footwall dome (Yin and Dunn, 1992; Dorsey and Becker, 1995; Dorsey and Roberts, 1996).

Stress State During Minidetachment and Whipple Detachment Fault Formation

Behr and Platt (2011) obtained steady-state differential stress $\Delta\sigma = 136 + 23/-17$ MPa during latest mylonitization, using quartz grain-size paleopiezometry ($\Delta\sigma$ likely was higher transiently). Ti-in-quartz thermobarometry and numerical modeling suggest that this $\Delta\sigma$ level was reached at ~9 km depth and 308 ± 40 °C (Behr and Platt, 2011), conditions remarkably similar to those determined for minidetachment embrittlement (Selverstone et al., 2012). The piezometer was calibrated in axisymmetric experiments ($\sigma_1 > \sigma_2 = \sigma_3$), but Whipple mylonites record mainly plane strain. Assuming "plane-stress" conditions ($\sigma_2 = [\sigma_1 + \sigma_3]/2$; Behr and Platt, 2013) allows a correction that increases $\Delta\sigma$ slightly, to $157 + 24/-19$ MPa, the value used in the Mohr construction (Fig. 4B). This correction affects the basic mechanical argument insignificantly.

For minidetachment and Whipple detachment fault formation at 9.5 km depth and hydrostatic pore pressure (Selverstone et al., 2012), horizontal planes (H in Fig. 4) would have had vertical effective normal traction $\sigma_v' = 154$ MPa (for rock density of 2650 kg/m^3 and water density of 1000 kg/m^3). Shear traction on plane H is unknown, but σ_v' on H locates the Mohr circle along the σ_n' axis as a function of Whipple detachment fault dip δ (Fig. 4B).

Initial Whipple Detachment Fault Dip in the Brittle-Plastic Transition

The Mohr construction yields (1) magnitudes and plunges of σ_1' ($\delta + 45°$; Fig. 4A) and σ_3',

(2) the ratio of shear to effective normal stress, τ/σ_n', on the Whipple detachment fault and minidetachments, and (3) the ratio τ/σ_{nR}' on Reidel shears, as a function of Whipple detachment fault dip δ and cohesion C_0 of intact mylonites (Figs. 4B; Appendix 1). A comparison of ratios (2) and (3) to appropriate laboratory-derived friction and cohesion levels (Fig. 5) provides independent limits on the nascent Whipple detachment fault dip as it formed and, thus, also the plunge of σ_1' (Figs. 4B and 5).

Ratio (2), τ/σ_n' on the nascent Whipple detachment fault, must equal or exceed static friction μ, which I assume was 0.6–0.85 for random-fabric quartzofeldspathic cataclasites (Luther et al., 2013; Byerlee, 1978; Beeler et al., 1996; Karner et al., 1997). Frictional fault slip obeys $\tau = \mu\sigma_n'$ (fault cohesion is negligible for the conditions of Whipple detachment fault formation: $\sigma_n' <$ 200 MPa; Byerlee, 1978; Axen, 2004). Using $\mu = 0.6$–0.85 limits initial Whipple detachment fault dip to 8°–26° for the parameter values used in Figure 4B. This corresponds to σ_1 plunging 53°–71° in the brittle-plastic transition (Fig. 5).

Ratio (3), τ/σ_{nR}' on R_2 shears that crosscut foliation, must equal or exceed internal friction

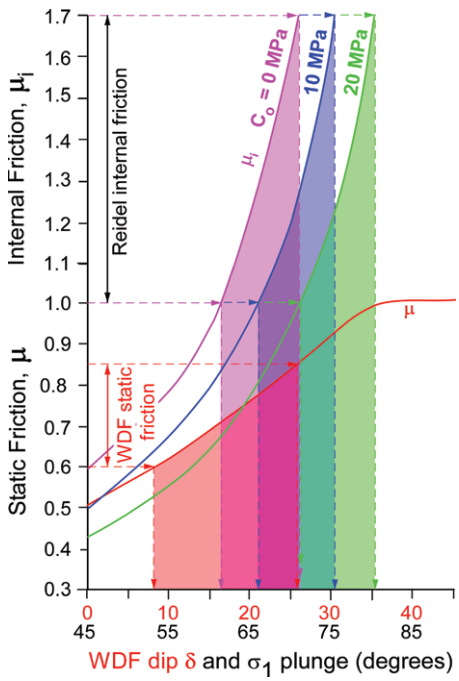

Figure 5. Plot of static friction μ on the Whipple detachment fault (WDF) and internal friction μ_i on Reidel shears (for three values of cohesion, C_0) vs. Whipple detachment fault dip (δ; red scale) and σ_1 plunge (black scale). Expected ranges of static and internal friction, and corresponding dips, are shown by dashed arrows and colors (see text and Appendix 1).

μ_i, which ranges from 1.0 to 1.7 for crystalline quartzofeldspathic rocks (Handin, 1966). Brittle failure of intact rock (R_2 shears) follows $\tau = C_0 + \mu_i\sigma_n'$, where cohesion C_0 of such rocks typically is 11–23 MPa (Handin, 1966). Cohesionless Reidel shears with $\mu_i = 1.0$–1.7 yield $\delta = 16°$–$26°$, increasing to $\delta = 21°$–$31°$ for $C_0 = 10$ MPa, and to $\delta = 26°$–$36°$ for $C_0 = 20$ MPa. The latter range does not overlap with the dip range obtained from Whipple detachment fault static friction $\mu = 0.6$–0.85 (Fig. 5).

Honoring both constraints (Whipple detachment fault static friction and R_2 internal friction) yields a favored initial Whipple detachment fault dip range of 16°–26°, with σ_1 plunging 61°–71° northeast (Fig. 5). This is similar to the angle inferred geologically between the Whipple detachment fault and the mylonite front (Davis, 1988; Lister and Davis, 1989; Behr and Platt, 2011).

Exploration of parameter combinations suggests that low (<30°) initial Whipple detachment fault dip is fairly robust. Table 1 shows Whipple detachment fault dip values consistent with static and internal friction ranges cited above ($\mu = 0.6$–0.85, $\mu_i = 1.0$–1.7), and for depths of 9, 9.5 (preferred), 10, and 11 km, cohesion $C_0 = 0$, 10, and 20 MPa, and the minimum, best, and maximum differential stress values (Behr and Platt, 2011, 2013). The high ends of dip ranges are limited by $\mu = 0.85$, and the low ends are limited by $\mu_i = 1.0$. For most parameter combinations, initial Whipple detachment fault dip δ is less than 30°, but a few combinations allow $\delta = 30°$–$45°$. However, such steep dips are not easily reconciled with the ~25° angle between the Whipple detachment fault and the mylonite front, nor with an initially gentle Whipple detachment fault dip between the mylonite front and Savahia Peak (see below), nor with the gentle angle at which the detachment cuts down across mylonites in the eastern footwall. Also, a high dip range is permitted for a depth of 11 km, but this depth is inconsistent with pressure of final mylonitization from both Behr and Platt (2011) and Selverstone et al. (2012). Thus, the high initial fault dips allowed by the Mohr construction are rejected. For several parameter combinations ($C_0 = 20$ MPa and/or $\Delta\sigma = 137$ MPa), no dip ranges satisfy both friction criteria. The lowest permissible dips (~5°–12°) are for $\Delta\sigma = 184$ MPa at 9 or 9.5 km depth, and none permits an initially horizontal Whipple detachment fault.

TABLE 1. MINIDETACHMENT AND WHIPPLE DETACHMENT FAULT DIP RANGES (DEGREES)

Depth (km)	C_0 (MPa)	Differential stress, $\Delta\sigma$ (MPa)		
		137	157	184
9	0	23–35	14–21	5–12
9	10	29–35	17–21	8–12
9	20	None*	21	12
9.5	0	27–45	16–26	8–15
9.5	10	36–45	21–26	11–15
9.5	20	None†	None*	14–15
10	0	35–45	20–31	10–18
10	10	None†	25–31	15–18
10	20	None†	30–31	17–18
11	0	None†	29–45	16–25
11	10	None†	39–45	19–25
11	20	None†	None†	24–25

*No dip ranges satisfy both $\mu_s = 0.6$–0.85 and $\mu_i = 1.0$–1.7.
†$\mu_i < 1.0$ for all dips up to 45°.

TECTONIC DRIVERS OF STRESS ROTATION DURING WHIPPLE DETACHMENT FAULT FORMATION

The mechanical analysis above requires explanation of why σ_1' was not vertical during Whipple detachment fault formation. Two possibilities exist: stress rotation within the mylonite zone and/or stress rotation at a crustal scale. Here, I review the regional tectonic history and conclude that both are permissible.

Maximum and minimum principal stresses during viscous simple shear are expected to be parallel to the infinitesimal strain axes, oriented 45° to the shear plane. Thus, the maximum and minimum principal stresses presumably were rotated within the late mylonitic shear zone while it was active, and as minidetachments and the Whipple detachment fault formed. If viscous flow were the only significant effect, then abrupt curvature of stress trajectories, and steepening of the initial Whipple detachment fault dip might be expected just above the mylonite front.

It is not obvious that the Whipple detachment fault steepened between the mylonite front and the west side of Savahia Peak, an upper-plate klippe ~10–12 km west of the mylonite front (Figs. 1B and 1C). This suggests that principal stresses well above the mylonite zone were not vertical, consistent with presence of thin mylonite zones for ~1 km above the mylonite front having dips similar to mylonites below (Davis, 1988). This suggests similar σ_1 orientation for ~1 km above the front. West of Savahia Peak, however, different mappers show different relationships. Carr et al. (1980) showed the Whipple detachment fault there dipping gently under Cenozoic strata and, farther north, under Cretaceous gneiss heavily intruded by Cenozoic dikes. Yin and Dunn (1992) also showed the Whipple detachment fault dipping gently below Cenozoic strata, but folded by a broad, NW-trending antiform-synform pair. Gans and Gentry (2016) presented convincing evidence that the basal Cenozoic nonconformity is preserved locally, and they suggested that the Whipple detachment fault and/or precursory normal faults were steep west of Savahia Peak.

Gradual stress-field rotation above the brittle-plastic transition is also consistent with the

known Whipple detachment fault fluid-pressure history. Inversion of minor fractures cutting the upper Whipple detachment fault footwall shows that σ_1 was subvertical above the gently dipping Whipple detachment fault in the upper brittle crust (Axen and Selverstone, 1994; Axen et al., 2015). Axen and Selverstone (1994), assuming vertical σ_1 and $\mu_s = 0.6$, showed that Whipple detachment fault slip at >4 km depth would require suprahydrostatic P_f, inconsistent with hydrostatic P_f to 9.5 km depth (Selverstone et al., 2012). This disparity is resolved if gradual stress rotation occurred from ~4 to 10 km depth, negating the need for gradual P_f increase over that depth range.

Crustal-scale stress rotation consistent with formation of primary low-angle normal faults emerges from static elastic models. Upward force applied to the base of the elastic crust may induce flexure that rotates the stress field (Fig. 2A; a buoyant crustal root was envisioned by Spencer and Chase, 1989). Similarly, shear traction applied to the base of the elastic crust (Yin, 1989) can cause crustal-scale stress rotation (Fig. 2B). Thus, high shear and differential stress levels in the pre–Whipple detachment fault mylonites (Behr and Platt, 2011) may have caused stress rotation well above the initially subhorizontal brittle-plastic transition.

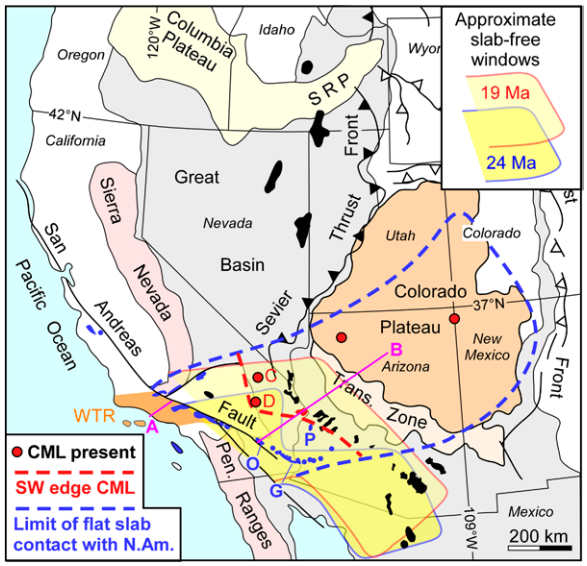

Figure 6. Simplified tectonic map of the western United States and adjacent Mexico (modern coordinates) showing Laramide and post-Laramide features discussed in text. The Whipple metamorphic core complex is in red beneath line A-B, which shows the location of the cross sections in Figure 7 (in present coordinates, where the SW end of the line is west of the San Andreas fault and beneath the western Transverse Ranges [WTR], which have been translated north and rotated clockwise ~110°; Dickinson, 1996). Also shown are: approximate locations of the slab window at 24 Ma and 19 Ma (from Atwater and Stock, 1998; McQuarrie and Oskin, 2010), the approximate limit of the area of contact between basal North America and the conjugate Shatsky Rise during Laramide time (Axen et al., 2018), continental mantle xenolith localities (C—Cima volcanic field, D—Dish Hill; Lee et al., 2001; Luffi et al., 2009), and the inferred location of the southwest edge of North American mantle lithosphere following Laramide subduction erosion. Orocopia and related schists are blue (O—Orocopia Mountains, G—Gavilan Hills, P—Plomosa Mountains). CML—continental mantle lithosphere; Pen. Ranges—Peninsular Ranges; SRP—Snake River Plain.

The regional tectonic history is consistent with both these models. It includes the following events. (1) Subduction of a buoyant oceanic plateau on the Farallon plate drove Laramide flat-slab subduction beneath southwestern North America (Fig. 6; Saleeby, 2003; Liu et al., 2010; Axen et al., 2018). Related subduction erosion removed lower crust and mantle lithosphere from beneath southern California and southwestern Arizona (Fig. 6). Thus, North American lithosphere tapered westward and presumably was progressively weaker to the west. (2) Subsequently, trench sediments were subducted, underplated, and metamorphosed to become the Rand-Pelona-Orocopia Schists, now exposed in tectonic windows beneath North American middle crust (Figs. 1A, 6, and 7A; Grove et al., 2003; Jacobson et al., 2007; Chapman, 2017). The Orocopia Schist was cooled rapidly and exhumed by several kilometers in each of two events, first in Eocene time (Fig. 7B) and further in late Oligocene–early Miocene time (Fig. 7C; Jacobson et al., 2007; Strickland et al., 2018). Late exhumation began ca. 28 Ma in the Gavilan Hills and ca. 24 Ma in the Orocopia Mountains (Figs. 1A and 6; Jacobson et al., 2007). (3) At ca. 28 Ma, the plate boundary changed from Farallon plate subduction under North America to a Pacific–North America dextral transform that lengthened through time (Atwater and Stock, 1998). The previously coherent Farallon plate began to fragment into smaller oceanic microplates (Monterrey, Arguello) at ca. 28 Ma, as recorded by clockwise rotation of Pacific microplate spreading directions (Bohannon and Parsons, 1995; Atwater and Stock, 1998). The microplates were sequentially "captured" by, and began moving with, the Pacific plate when microplate spreading ceased, first at ca. 18 Ma (Atwater and Stock, 1998). (4) Microplate motions suggest that slab windows opened between them and the inexorably sinking Farallon slab as early as ca. 28 Ma, while microplate subduction continued slowly, but well before they were captured by the Pacific plate (Atwater and Stock, 1998). Hot, buoyant asthenosphere probably flowed upward into slab-free windows under southern California and southwestern Arizona, contacting North American crust and/or mantle lithosphere (Fig. 7C; Severinghaus and Atwater, 1990; Atwater and Stock, 1998) and triggering both extension and magmatism in the region.

This tectonic evolution yields two mutually compatible scenarios that could have caused crustal-scale stress rotation in southern California:

(1) Rising, buoyant asthenosphere (Figs. 6 and 7C; Severinghaus and Atwater, 1990; Atwater and Stock, 1998) flexed and heated the thinned and weakened marginal North American lithosphere (Spencer and Chase, 1989). First-order isostatic buoyancy calculations (Appendix 2) indicate that this can provide sufficient upward force. Slab rollback and re-establishment of an asthenospheric wedge or northward migration of the Mendocino fracture zone under southern Arizona (e.g., Glazner and Bartley, 1984) probably had similar consequences. Atwater and Stock (1998) mapped the ca. 28 Ma slab-free window as a narrow, coast-parallel tear in the slab, located west of modern schist exposures along the San Andreas fault, with an east-trending projection under the Gavilan Hills area (Fig. 6) and southwestern Arizona (these tears are not shown in Fig. 6).

(2) Shear stress applied to basal North America by pre–Whipple detachment fault mylonitic flow or by captured microplates may have driven crustal-scale stress rotation. However, basal shear stress applied by microplates is rejected for several reasons. First, the earliest microplate capture occurred ca. 18 Ma, well after extensional exhumation began in the Colorado River extensional corridor (ca. 21–22 Ma), so an 18 Ma event could not have triggered earlier extension. Second, once captured, microplates moved northwest relative to North America (Bohannon and Parsons, 1995; Atwater and Stock, 1998), about perpendicular to the top-to-the-NE transport of low-angle normal faults in the Colorado River extensional corridor. Top-to-the-NW basal shear traction would not have caused formation of top-to-the-NE low-angle normal faults. Third,

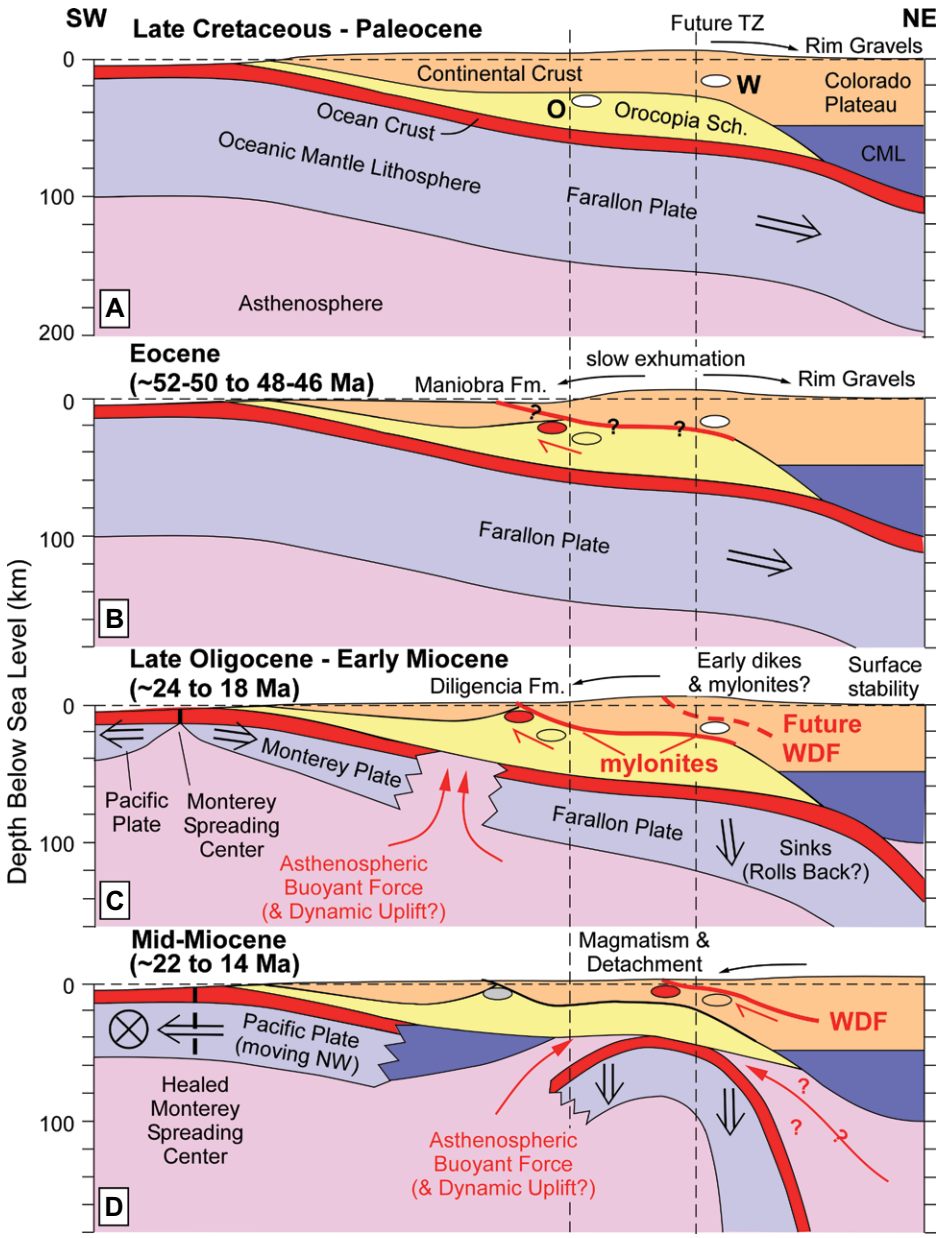

Figure 7. Conceptual cross sections along line A-B in Figure 6, showing preferred tectonic evolution of the study area (no vertical exaggeration). Location of west edge of continental mantle lithosphere (CML) is uncertain. Ovals show locations of rocks now exposed in the Whipple (W) and Orocopia (O) Mountains at times before (white), during (red), and after (gray) tectonic activity (unfilled ovals show prior locations). Red fault shown in the Eocene panel is speculative; exhumation of Orocopia Schist then may have been erosional (Jacobson et al., 2007). Velocities of oceanic plates relative to North America are shown schematically by arrows (circle with cross shows motion away from reader). Thin arrows above land surface show sediment transport. Dashed vertical reference lines are tied to stable North America. TZ—transition zone (Fig. 6). See text for discussion and references.

before earliest capture (from ca. 28–18 Ma), microplates continued to subduct generally eastward, applying the wrong sense of shear to basal North America. Last, known microplate remnants beneath marginal North America do not extend far inland (Nicholson et al., 1994; Brothers et al., 2012), so they were too far west to apply basal shear below the Colorado River extensional corridor.

My preferred tectonic evolution appeals to both upward basal forces and basal shear traction. (1) Early Laramide subduction erosion thinned and weakened marginal North American lithosphere, preparing it for low-angle normal fault formation due to crustal flexure. The approximate west edge of strong continental mantle lithosphere is shown in Figure 6 (dashed red line), on the basis of xenolith studies (Lee et al., 2001; Luffi et al., 2009) and Orocopia Schist exposures (where North American basal crust and mantle lithosphere are absent). The Orocopia Schist in the Plomosa Mountains (Figs. 1A and 6), only ~50 km south of the Whipple detachment fault (Strickland et al., 2018), suggests that the west edge of strong North American mantle lithosphere was near the future Whipple metamorphic core complex. Final exhumation by the top-to-the-NE Plomosa detachment was synchronous with activity on other Colorado River extensional corridor low-angle normal faults (Strickland et al., 2018).

(2) Underplating of Orocopia Schist probably caused surface uplift and erosion in the transition zone (Figs. 7A and 7B), consistent with Eocene geological events: cooling and significant exhumation of Orocopia Schist (Fig. 7B; Jacobson et al., 2007), slow, partial exhumation of the Whipple footwall (Anderson, 1996), northeast transport of Rim Gravels sourced in the transition zone (Elston and Young, 1991), and deposition of the marine Maniobra Formation in the Orocopia Mountains. Deposition of Rim Gravels ceased well before onset of Colorado River extensional corridor extension: the gravels underwent a period of deep soil formation and very minor erosion between ca. 46–48 and 24 Ma (Elston and Young, 1991), suggesting that the crustal thickness in the transition zone had been reduced to values comparable to the adjacent Colorado Plateau.

(3) At ca. 28 Ma, tectonic exhumation of the Orocopia Schist in the Gavilan Hills (Fig. 6) was renewed due to top-to-the-E slip on the low-angle Gatuna fault (Jacobson et al., 2002, 2007). I infer that this was in response to asthenospheric upwelling in the east-trending tear in the slab at 28 Ma (discussed above; Atwater and Stock, 1998). The schist cooled from ~300–350 °C to ~150–200 °C in this event, corresponding to ~11–17 km of exhumation (Jacobson et al., 2007). Similar rapid cooling and exhumation of the schist in the Orocopia Mountains began at ca. 24 Ma, due to top-to-the-NE slip on the Orocopia detachment fault and a thin, subjacent mylonite zone (Fig. 7C; Jacobson et al., 2007). This also probably occurred in response to asthenospheric ascent through the growing slab-free window (Figs. 6 and 7C).

I conclude that the related mylonite zone continued at depth northeast below the Colorado River extensional corridor (Fig. 7C), where it is now exposed in mylonite fronts (Davis, 1988;

Singleton and Mosher, 2012). Thus, early Miocene mylonitic flow probably applied top-to-the-NE basal shear to the Colorado River extensional corridor, driving the stress rotation required to form the low-angle normal faults in the area.

(4) Eastward expansion of the slab-free window, and/or other sinking-slab mechanisms, triggered magmatism in the Whipple Mountains beginning ca. 24 Ma (becoming voluminous by ca. 21–19 Ma; Gans and Gentry, 2016), and extension throughout the Colorado River extensional corridor beginning ca. 22–21 Ma (Fig. 7D). By ca. 19 Ma, the slab-free window probably fully underlay the Colorado River extensional corridor (Fig. 6; Atwater and Stock, 1998; McQuarrie and Oskin, 2010), applying upward force to the base of the Colorado River extensional corridor and favoring low-angle normal fault formation there.

DISCUSSION

Controls on Strength and Embrittlement

The model suggests that onset of cataclasis caused immediate frictional strengthening from ~0.3 to 0.6–0.85. Such an evolution may be common and may keep the brittle-plastic transition strong. During retrograde mylonitic shearing in the Whipple Mountains, aligned, frictionally weak phyllosilicate minerals formed on mylonite planes (e.g., Behr and Platt, 2011), and subsequent cataclasis exploited these planes (Selverstone et al., 2012). Chlorite-coated C-planes probably had $\mu = 0.27–0.32$ if wet, or higher if nominally dry ($\mu = 0.42–0.68$; possible if hydration reactions consumed all free water; Behnsen and Faulkner, 2012). The random-fabric quartzofeldspathic cataclasites and pseudotachylyte that formed on minidetachments (Selverstone et al., 2012) and the Whipple detachment fault (Luther et al., 2013) require normal friction (0.6–0.85). Such embrittlement strengthening also may occur when upper plates of thrusts exit the brittle-plastic transition, or when shear-strain rate increases in brittle-plastic transition shear zones. Formation of weak clays in brittle fault zones likely is a common fault-weakening mechanism, but this appears not to have happened along the Whipple detachment fault until the footwall was juxtaposed at shallow crustal levels beneath clay-bearing upper-plate strata (see above).

Thus, geochemical-mineralogical controls on the mechanics of the crustal strength maximum can be as important as *P* and *T* changes. Selverstone et al. (2012) concluded that metamorphic crystallization of strong, retrograde epidote probably strengthened mylonites, ending mylonitic flow and favoring frictional-cataclastic minidetachment slip. Late-mylonitic epidote and chlorite, with high water contents, may have scavenged free water and enhanced the trend toward hydrostatic P_f and high frictional strength. Free water as a transport pathway on grain boundaries aids mylonitic dissolution-precipitation reactions, but mylonite porosity is expected to be low (<1%). Thus, retrograde phases may have consumed sufficient water to slow or stop diffusive flux, retard mylonitic flow, and further encourage cataclasis, which, through dilatancy, would cause P_f levels to plummet.

The importance of fluids in the brittle-plastic transition has been noted for other low-angle normal faults. Minor, semipenetratively developed fractures formed at abnormally high temperature during evolution of the low-angle, normal Brenner Line, largely ending mylonitization (Axen et al., 2001). Similarly, an along-strike change of fluid composition partly controlled the embrittlement and structural style of the Simplon Line footwall (Wawrzyniec et al., 1999).

Application of the Model to Other Low-Angle Normal Faults

The mechanical-tectonic model may apply in its entirety to other Colorado River extensional corridor low-angle normal faults, which also have dominantly quartzofeldspathic footwalls and so presumably are also strong (cataclasites have not been described in detail from other Colorado River extensional corridor footwalls). These low-angle normal faults were formed coeval with the Whipple detachment fault and were kinematically coordinated, lending support to a common tectono-mechanical origin. Mylonitic anisotropy (required by this model) in the form of mylonitic foliation is common in other Colorado River extensional corridor footwalls (e.g., Howard and John, 1987; Singleton and Mosher, 2012), but minidetachments have not (yet?) been described.

Many other North American low-angle normal faults also have the needed mylonitic anisotropy, but their locally differing transport directions (Fig. 1A) and/or ages (e.g., Axen et al., 1993) suggest that different drivers of stress rotation may apply. Suprasubduction low-angle normal faults, such as in the Aegean (e.g., Lister et al., 1984), form where slab rollback may cause buoyant forces and upper-plate flexural stresses. One potential test of the applicability of this model is to search for minidetachments preserved beneath other strong low-angle normal faults.

Implications for Numerical Models of Metamorphic Core Complexes

Many numerical models of metamorphic core complex evolution yield reasonable final geometries (e.g., Lavier et al., 1999; Choi et al., 2013) but do not produce primary low-angle normal faults. Such models typically have symmetric boundary conditions, use initially isotropic media "seeded" with one or more defects on which faults nucleate, and impose displacement weakening (progressively reduced friction or cohesion) that favors shear localization. These conditions contrast with the asymmetric boundary conditions, mylonitic anisotropy, and embrittlement strengthening of the model presented here and those upon which it is built (Spencer and Chase, 1989; Yin, 1989). Strong faults are needed for upper-plate rider blocks to be sequentially produced, isostatically rotated, and abandoned (Choi et al., 2013), but that history is lacking in many well-studied metamorphic core complexes. These factors suggest that asymmetric boundary conditions on the elastic-frictional crust may be necessary for formation of strong low-angle normal faults.

Crustal and Seismogenic Zone Thickness

Low-angle normal fault formation may be favored in thick, hot, orogenic crust (e.g., Whitney et al., 2013). However, Laramide subduction erosion below and west of the transition zone apparently removed North American mantle lithosphere and any older, overthickened crustal root. This factor, plus evidence for slow exhumation in the transition zone and Colorado Plateau (Figs. 7A and 7B; discussed above) prior to Colorado River extensional corridor extension, suggests that Colorado River extensional corridor (transition zone) crustal thickness was comparable to the adjacent craton (Colorado Plateau) at the onset of extension. If asthenospheric rise into a slab-free window triggered extensional exhumation of the Orocopia Schist and extension and magmatism in the Colorado River extensional corridor, then hot and weak, but not necessarily overthickened, crust may have been needed to form the strong low-angle normal faults.

Thin seismogenic zones likely characterize even strong low-angle normal fault terrains and may help to explain the paucity of large low-angle normal fault earthquakes (Jackson and White, 1989; Collettini and Sibson, 2001). Heat advected with rising low-angle normal fault footwalls thins the crustal seismogenic zone. The Whipple detachment fault seismogenic zone probably was only ~6–8 km thick, with its base defined by the brittle-plastic transition at 9–10 km depth and 300–400 °C (Behr and Platt, 2011; Selverstone et al., 2012), while weak, velocity-strengthening clay gouge likely defined the top. To my knowledge, clay-bearing gouge is found along the Whipple detachment fault (Fig. 3B; Haines and van der Pluijm, 2012)

only where it probably was derived from upper-plate basins ≤2–3 km thick (Carr et al., 1980; Yin and Dunn, 1992; Dorsey and Becker, 1995; Gans and Gentry, 2016). Clays are negligible in Whipple detachment fault footwall cataclasites (Luther et al., 2013). This thin seismogenic zone, especially its shallow base, may limit low-angle normal fault seismic moment release.

CONCLUSIONS

The Whipple detachment fault formed progressively as a strong low-angle normal fault in the brittle-plastic transition (crustal strength maximum) at ~9–10 km depth and ~300–400 °C. It was not a Coulomb fracture, but it was oriented ~45° to the maximum principal stress and slipped under maximum ambient shear stress, ~80 MPa. The Whipple detachment fault probably had Byerlee rock friction (0.6–0.85) in the depth range ~9–10 to 2–3 km. Minidetachments were formed by frictional slip on preexisting mylonitic foliation, and some linked to form the Whipple detachment fault, which propagated upward in the brittle crust at low dip, maintained by progressive isostatic footwall rebound. Accumulating slip smoothed the steps left from misaligned minidetachments and contributed to formation of the fractured damage zone and fault core.

The transition from mylonitic shearing to frictional minidetachment slip on mylonitic C planes was triggered by retrograde crystallization of strong epidote. Initial static friction on chlorite-coated C planes was probably low (~0.3), but subsequent cataclasis created frictionally stronger (0.6–0.85) random-fabric quartzofeldspathic cataclasites, ultracataclasites, and pseudotachylyte. Retrograde chlorite and epidote likely scavenged free water, contributing to early fluid pressure drop, but dilatancy upon embrittlement increased porosity, causing pore-fluid pressure on minidetachments to drop from lithostatic to hydrostatic levels, which also presumably characterized Whipple detachment fault formation.

The maximum principal stress plunged ~60°–70° NE, and the Whipple detachment fault dipped ~15°–25° NE while forming in the brittle-plastic transition. Stress-field rotation probably extended a few kilometers above the mylonite zone, due to basal shear stress and/or flexure caused by buoyant asthenospheric rise into slab-free windows. Laramide subduction erosion thinned and weakened marginal North American lithosphere, enhancing flexure and stress-field rotation. This probably occurred first in the Orocopia Mountains, where top-to-the-NE mylonitization and detachment faulting are slightly older. The detachment-related Orocopia mylonite zone probably thickened with depth and extended east below the Colorado River extensional corridor, where it was captured by evolving low-angle normal faults and exposed at mylonite fronts. Shear applied by this mylonite zone to the base of the brittle-elastic Colorado River extensional corridor crust may also have contributed to stress-field rotation and low-angle normal fault formation.

APPENDIX 1: WHIPPLE DETACHMENT FAULT STATIC FRICTION AND REIDEL SHEAR INTERNAL FRICTION

The Mohr construction (Fig. 4B) yields expressions for the ratios of shear to normal traction on the Whipple detachment fault and on Reidel shears as functions of detachment dip. These ratios must equal or exceed the static friction μ of the Whipple detachment fault or the internal friction μ_i of R_2 shears, respectively.

Stress magnitudes known independently are the differential stress $\Delta\sigma$ (Behr and Platt, 2011, 2013) and the effective vertical stress σ_v' on horizontal plane *H* in the brittle-plastic transition (at ~9.5 km depth; Selverstone et al., 2012). The detachment dip, δ, is constrained somewhat loosely by geologic data and is treated here as a free variable to be determined independently.

From Figure 4B, the magnitude of shear traction on the Whipple detachment fault is given by:

$$\left|\tau_{max}\right| = \Delta\sigma / 2. \quad (1)$$

Effective normal stress on the Whipple detachment fault is given by:

$$\sigma_m' = \sigma_v' - \left(\Delta\sigma/2\right)\sin\left(2\delta\right) = \left[\rho_c g z\left(1-\lambda\right)\right] - \left(\Delta\sigma/2\right)\sin\left(2\delta\right), \quad (2)$$

where σ_m' is the effective mean stress, ρ_c is crustal density (2650 kg/m^3), g is gravity, *z* is depth (9500 m), λ is the fluid-pressure factor, given for hydrostatic conditions by the density of pore fluid divided by crustal density (λ = 1000/2650 = 0.377), and δ is the detachment dip.

Combining Equations 1 and 2 gives

$$\mu = \tau_{max} / \sigma_m' = \Delta\sigma / \left[2\rho_c g z\left(1-\lambda\right) - \Delta\sigma\sin\left(2\delta\right)\right]. \quad (3)$$

Equation 3 is plotted in Figure 5 for detachment dips of 0–45°. Fault cohesion is ignored for effective normal stress <200 MPa (Byerlee, 1978; Axen, 2004).

For Reidel shears, both the internal friction and cohesion C_0 of intact rock must be considered (Fig. 4B). R_2 shears cut across foliation, so they formed in intact rock (in contrast, some or all R_1 shears likely followed chlorite-coated C′ mylonitic planes). Failure follows $\tau = \mu_i\sigma_{nR}' + C_0$, where μ_i is given by the tangent of the angle of internal friction ϕ_i, so

$$\tau = \left(\tan\phi_i\right)\sigma_{nR}' + C_0. \quad (4)$$

The parametric equations for traction on Reidel shears are:

$$\sigma_{nR}' = \sigma_m' - \left(\Delta\sigma/2\right)\cos\left(2\theta_R\right), \quad (5)$$

and

$$\text{and } \tau = \left(\Delta\sigma/2\right)\sin\left(2\theta_R\right), \quad (6)$$

where θ_R is the angle between σ_1 and the Reidel shear. From triangle a-σ_m'-R, we see that $2\theta_R = 90 - \phi_i$, so these become:

$$\sigma_n' = \sigma_m' - \left(\Delta\sigma/2\right)\sin\left(\phi_i\right), \quad (5a)$$

and

$$\text{and } \tau = \left(\Delta\sigma/2\right)\cos\left(\phi_i\right). \quad (6a)$$

Substituting Equation 5a into Equation 4, equating it to the right-hand side of Equation 6a, and rearranging gives:

$$C_0 = \left(\Delta\sigma/2\right)\cos\left(\phi_i\right) - \tan\left(\phi_i\right)\left[\sigma_m' - \left(\Delta\sigma/2\right)\sin\left(\phi_i\right)\right]. \quad (7)$$

The effective mean stress, σ_m' (Eq. 2), is substituted into Equation 7. The resulting equation is then solved iteratively for ϕ_i, yielding μ_i and the internal friction curves shown in Figure 5 for values of C_0 of 0, 10, and 20 MPa.

APPENDIX 2: ISOSTATIC BUOYANCY DUE TO UPWARD ASTHENOSPHERIC FLOW

Can isostatic buoyancy comparable to that from a crustal root be caused by upward flow of asthenosphere into an opening slab-free window? For a 20-km-thick crustal root, I consider lower crust with density range of ρ_{lc} = 2900–3000 kg/m^3 and a continental mantle lithosphere density range of ρ_{cml} = 3200–3250 kg/m^3. This yields a density difference $\Delta\rho$ = 200–350 kg/m^3. The buoyant upward stress is then given by $\Delta\rho g$(20,000 m) = 39–69 MPa.

For the slab-free window, I consider a range of oceanic lithosphere thicknesses, based upon the age of ocean lithosphere at the west edge of the window when the tear developed, as shown by Atwater and Stock (age of 13–6 m.y.; obtained by subtracting the age of the magnetic chron at the ridge from the age of the chron at the edge of the window at that time). These are then converted into a reasonable range of oceanic lithosphere thicknesses t_{ol} = 35–60 km (Alfonso et al., 2007; Kumar and Kawakatsu, 2011). I assume ocean crust surrounding the opening window had standard thickness t_{oc} = 7 km (the thicker conjugate Shatsky Rise was farther east when slab-free windows opened), leaving a range of oceanic mantle lithosphere thickness t_{oml} = 28–53 km. The Farallon plate crust presumably was metamorphosed to (at least) amphibolite grade (the typical grade of exposed, overlying Orocopia Schist; e.g., Jacobson et al., 2007), with density ρ_{oc} = 3000 kg/m^3 (average of 68 amphibolite samples from Smithson, 1971). I assume that the density of oceanic mantle lithosphere is ρ_{oml} = 3300 kg/m^3, and that of asthenosphere is ρ_a = 3170–3200 kg/m^3 (Niu and Batiza, 1991; for 40 km depth and 5% melt extracted).

The mass of a (1 m^2) column of oceanic lithosphere is given by:

$$\left(7000\,\text{m}\right)\rho_{oc} + t_{oml}\rho_{oml}. \quad (8)$$

This yields masses of 113×10^6 kg or 196×10^6 kg for 35- or 60-km-thick ocean lithosphere, respectively.

The mass of an equivalent column of asthenosphere is given by:

$$t_a\rho_a, = 111 - 112 \times 10^6 \text{ kg (or } 190 - 192 \times 10^6 \text{ kg)} \quad \text{for } t_a = 35 \text{ (or 60) km}. \quad (9)$$

Combining these values yields buoyant upward stress = 38–56 MPa for 60 km columns, or 14–24 MPa for 35 km columns.

Thus, asthenosphere filling a 60-km-thick window will provide 56%–142% of the upward buoyancy of a 20-km-thick crustal root, and asthenosphere filling even a 35-km-thick slab-free window will supply 20%–60% of the buoyant upward stress of a 20 km crustal root.

ACKNOWLEDGMENTS

Reviews by and/or discussion with John Platt, Alex Rinehart, Brandon Lutz, and anonymous reviewers are appreciated. This study was funded by National Science Foundation grant EAR-1348076.

REFERENCES CITED

Alfonso, J.C., Ranalli, G., and Fernández, M., 2007, Density structure and buoyancy of the oceanic lithosphere revisited: Geophysical Research Letters, v. 34, L10302, https://doi.org/10.1029/2007GL029515.

Anderson, E.M., 1942, The Dynamics of Faulting and Dyke Formation with Application to Britain: Edinburgh, UK, Oliver and Boyd, 191 p.

Anderson, J.L., 1996, Status of thermobarometry in granitic batholiths: Transactions of the Royal Society of Edinburgh–Earth Sciences, v. 87, p. 125–138, https://doi.org/10.1017/S0263593300006544.

Anderson, J.L., Barth, A., and Young, E., 1988, Mid-crustal Cretaceous roots of Cordilleran metamorphic core complexes: Geology, v. 16, p. 366–369, https://doi.org/10.1130/0091-7613(1988)016<0366:MCCROC>2.3.CO;2.

Atwater, T., and Stock, J., 1998, Pacific–North America plate tectonics of the Neogene southwestern United States: International Geology Review, v. 40, p. 375–402, https://doi.org/10.1080/00206819809465216.

Axen, G.J., 1993, Ramp-flat detachment faulting and low-angle normal reactivation of the Tule Springs thrust, southern Nevada: Geological Society of America Bulletin, v. 105, p. 1076–1090, https://doi.org/10.1130/0016-7606(1993)105<1076:RFDFAL>2.3.CO;2.

Axen, G.J., 2004, Mechanics of low-angle normal faults, *in* Karner, G.D., Taylor, B., Driscoll, N.W., and Kohlstedt, D.L., eds., Rheology and Deformation of the Lithosphere at Continental Margins: New York, Columbia University Press, p. 46–91, https://doi.org/10.7312/karn12738-004.

Axen, G.J., and Bartley, J.M., 1997, Field tests of rolling hinges: Existence, mechanical types and implications for extensional tectonics: Journal of Geophysical Research, v. 102, p. 20515–20537, https://doi.org/10.1029/97JB01355.

Axen, G.J., and Selverstone, J., 1994, Stress state and fluid-pressure level along the Whipple detachment fault, California: Geology, v. 22, p. 835–838, https://doi.org/10.1130/0091-7613(1994)022<0835:SSAFPL>2.3.CO;2.

Axen, G.J., Wernicke, B.P., Skelly, M.F., and Taylor, W.J., 1990, Mesozoic and Cenozoic tectonics of the Sevier thrust belt in the Virgin River Valley area, southern Nevada, *in* Wernicke, B.P., ed., Basin and Range Extensional Tectonics at the Latitude of Las Vegas, Nevada: Geological Society of America Memoir 176, p. 123–154, https://doi.org/10.1130/MEM176-p123.

Axen, G.J., Taylor, W.M., and Bartley, J.M., 1993, Space-time patterns and tectonic controls of Tertiary extension and magmatism in the Great Basin of the western United States: Geological Society of America Bulletin, v. 105, p. 56–76, https://doi.org/10.1130/0016-7606(1993)105<0056:STPATC>2.3.CO;2.

Axen, G.J., Selverstone, J., and Wawrzyniec, T., 2001, High-temperature embrittlement of extensional Alpine mylonite zones in the midcrustal ductile-brittle transition: Journal of Geophysical Research, v. 106, p. 4337–4348, https://doi.org/10.1029/2000JB900372.

Axen, G.J., Luther, A., and Selverstone, J., 2015, Paleostress directions near two low-angle normal faults: Testing mechanical models of weak faults and off-fault damage: Geosphere, v. 11, p. 1996–2014, https://doi.org/10.1130/GES01211.1.

Axen, G.J., van Wijk, J.W., and Currie, C.A., 2018, Basal continental mantle lithosphere displaced by flat-slab subduction: Nature Geoscience, v. 11, p. 961–964, https://doi.org/10.1038/s41561-018-0263-9.

Beeler, N.M., Tullis, T.E., Blanpied, M.L., and Weeks, J.D., 1996, Frictional behavior of large-displacement experimental faults: Journal of Geophysical Research, v. 101, p. 8697–8715, https://doi.org/10.1029/96JB00411.

Behnsen, J., and Faulkner, D.R., 2012, The effect of mineralogy and effective normal stress on frictional strength of sheet silicates: Journal of Structural Geology, v. 42, p. 49–61, https://doi.org/10.1016/j.jsg.2012.06.015.

Behr, W.M., and Platt, J.P., 2011, A naturally constrained stress profile through the middle crust in an extensional terrain: Earth and Planetary Science Letters, v. 303, p. 181–192, https://doi.org/10.1016/j.epsl.2010.11.044.

Behr, W.M., and Platt, J.P., 2013, Rheological evolution of a Mediterranean subduction complex: Journal of Structural Geology, v. 54, p. 136–155, https://doi.org/10.1016/j.jsg.2013.07.012.

Block, L., and Royden, L.H., 1990, Core complex geometries and regional scale flow in the lower crust: Tectonics, v. 9, p. 557–567, https://doi.org/10.1029/TC009i004p00557.

Bohannon, R.G., and Parsons, T., 1995, Tectonic implications of post–30 Ma Pacific and North American relative plate motions: Geological Society of America Bulletin, v. 107, p. 937–959, https://doi.org/10.1130/0016-7606(1995)107<0937:TIOPMP>2.3.CO;2.

Brace, W.F., and Kohlstedt, D.L., 1980, Limits on lithospheric stress imposed by laboratory experiments: Journal of Geophysical Research, v. 85, p. 6248–6252, https://doi.org/10.1029/JB085iB11p06248.

Brothers, D., Harding, A., González-Fernández, A., Holbrook, W.S., Kent, G., Driscoll, N., Fletcher, J., Lizzaralde, D., Umhoeffer, P., and Axen, G., 2012, Farallon slab detachment and deformation of the Magdalena Shelf, southern Baja California: Geophysical Research Letters, v. 39, L09307, https://doi.org/10.1029/2011GL050828.

Buck, W.R., 1988, Flexural rotation of normal faults: Tectonics, v. 7, p. 959–973, https://doi.org/10.1029/TC007i005p00959.

Burchfiel, B.C., Zhiliang, C., Hodges, K.V., Yuping, L., Royden, L.H., Changrong, D., and Jiene, X., 1992, The South Tibetan Detachment System, Himalayan Orogen: Extension Contemporaneous With and Parallel To Shortening in a Collisional Mountain Belt: Geological Society of America Special Paper 269, 42 p.

Byerlee, J., 1978, Friction of rocks: Pure and Applied Geophysics, v. 116, p. 615–626, https://doi.org/10.1007/BF00876528.

Carr, W.J., Dickey, D.D., and Quinlivan, W.D., 1980, Geological Map of the Vidal NW, Vidal Junction, and Parts of the Savahia Peak SW and Savahia Peak Quadrangles, San Bernardino County, California: U.S. Geological Survey Miscellaneous Field Investigations Map I-1126, scale 1:24,000.

Chapman, A.D., 2017, The Pelona-Orocopia-Rand and related schists of southern California: A review of the best-known archive of shallow subduction on the planet: International Geology Review, v. 59, no. 5-6, p. 664–701, https://doi.org/10.1080/00206814.2016.1230836.

Choi, E., Buck, W.R., Lavier, L.L., and Dinesen Petersen, K., 2013, Using core complex geometry to constrain fault strength: Geophysical Research Letters, v. 40, p. 3863–3867, https://doi.org/10.1002/grl.50732.

Collettini, C., 2011, The mechanical paradox of low-angle normal faults: Current understanding and open questions: Tectonophysics, v. 510, p. 253–268, https://doi.org/10.1016/j.tecto.2011.07.015.

Collettini, C., and Sibson, R.H., 2001, Normal faults, normal friction?: Geology, v. 29, p. 927–930, https://doi.org/10.1130/0091-7613(2001)029<0927:NFNF>2.0.CO;2.

Collettini, C., De Paola, N., Holdsworth, R.E., and Barchi, M.R., 2006, The development and behavior of low-angle normal faults during Cenozoic asymmetric extension in the northern Apennines, Italy: Journal of Structural Geology, v. 28, p. 333–352, https://doi.org/10.1016/j.jsg.2005.10.003.

Crittenden, M.D., Jr., Coney, P.J., and Davis, G.H., 1980, Cordilleran Metamorphic Core Complexes: Geological Society of America Memoir 153, 491 p.

Davis, G.A., 1988, Rapid upward transport of mid-crustal mylonitic gneisses in the footwall of a Miocene detachment fault, Whipple Mountains, southeastern California: Geologische Rundschau, v. 77, p. 191–209, https://doi.org/10.1007/BF01848684.

Davis, G.A., and Lister, G.S., 1988, Detachment faulting in continental extension; perspectives from the southwestern U.S. Cordillera, *in* Clark, S.P., Jr., Burchfiel, B.C., and Suppe, J., eds., Processes in Continental Lithospheric Deformation: Geological Society of America Special Paper 218, p. 133–159.

Davis, G.A., Lister, G.S., and Reynolds, S.J., 1986, Structural evolution of the Whipple and South Mountains shear zones, southwestern United States: Geology, v. 14, p. 7–10, https://doi.org/10.1130/0091-7613(1986)14<7:SEOTWA>2.0.CO;2.

Dickinson, W.R., 1996, Kinematics of Transrotational Tectonism in the California Transverse Ranges and its Contribution to Cumulative Slip along the San Andreas Transform System: Geological Society of America Special Paper 305, 46 p.

Dorsey, R.J., and Becker, U., 1995, Evolution of a large Miocene growth structure in the upper plate of the Whipple detachment fault, northeastern Whipple Mountains, California: Basin Research, v. 7, p. 151–163, https://doi.org/10.1111/j.1365-2117.1995.tb00101.x.

Dorsey, R.J., and Roberts, P., 1996, Evolution of the Miocene north Whipple basin in the Aubrey Hills, western Arizona, upper plate of the Whipple detachment fault, *in* Beratan, K.K., ed., Reconstructing the History of Basin and Range Extension Using Sedimentology and Stratigraphy: Geological Society of America Special Paper 303, p. 127–146, https://doi.org/10.1130/0-8137-2303-5.127.

Elston, D.P., and Young, R.A., 1991, Cretaceous–Eocene (Laramide) landscape development and Oligo-Pliocene drainage reorganization of the transition zone and Colorado Plateau, Arizona: Journal of Geophysical Research, v. 96, p. 12389–12406, https://doi.org/10.1029/90JB01978.

Faulkner, D.R., Jackson, C.A.L., Lunn, R.J., Schlische, R.W., Shipton, Z.K., Wibberley, C.A.J., and Withjack, M.O., 2010, A review of recent developments concerning the structure, mechanics and fluid flow properties of fault zones: Journal of Structural Geology, v. 32, p. 1557–1575, https://doi.org/10.1016/j.jsg.2010.06.009.

Foster, D.A., and John, B.E., 1999, Quantifying tectonic exhumation in an extensional orogen with thermochronology: Examples from the southern Basin and Range Province, *in* Ring, U., Brandon, M.T., Lister, G.S., and Willett, S.D., eds., Exhumation Processes: Normal Faulting, Ductile Flow and Erosion: Geological Society [London] Special Publication 154, p. 343–364, https://doi.org/10.1144/GSL.SP.1999.154.01.16.

Gans, P.B., and Gentry, B.J., 2016, Dike emplacement, footwall rotation, and the transition from magmatic to tectonic extension in the Whipple Mountains metamorphic core complex, southeastern California: Tectonics, v. 35, p. 2564–2608, https://doi.org/10.1002/2016TC004215.

Garcés, M., and Gee, J.S., 2007, Paleomagnetic evidence of large footwall rotations associated with low-angle normal faults at the Mid-Atlantic Ridge: Geology, v. 35, p. 279–282, https://doi.org/10.1130/G23165A.1.

Gawthorpe, R.L., and Leeder, M.R., 2000, Tectono-sedimentary evolution of active extensional basins: Basin Research, v. 12, p. 195–218, https://doi.org/10.1046/j.1365-2117.2000.00121.x.

Glazner, A.F., and Bartley, J.M., 1984, Timing and tectonic setting of Tertiary low-angle normal faulting and associated magmatism in the southwestern United States: Tectonics, v. 3, p. 385–396, https://doi.org/10.1029/TC003i003p00385.

Griffith, W.A., 2016, How dynamic weakening makes faults stronger: The role of melting in post-seismic healing: Geology, v. 44, p. 1063–1064, https://doi.org/10.1130/focus122016.1.

Grove, M., Jacobson, C.E., Barth, A.P., and Vucic, A., 2003, Temporal and spatial trends of Late Cretaceous–Early Tertiary underplating of Pelona and related schist

beneath southern California and southwestern Arizona, *in* Johnson, S.E., Paterson, S.R., Fletcher, J.M., Girty, G.H., Kimbrough, D.L., and Martín-Barajas, A., eds., Tectonic Evolution of Northwestern Mexico and the Southwestern USA: Geological Society of America Special Paper 374, p. 381–406, https://doi.org/10.1130/0-8137-2374-4.381.

Haines, S.H., and van der Pluijm, B.A., 2012, Patterns of mineral transformations in clay gouge, with examples from low-angle normal fault rocks in the western USA: Journal of Structural Geology, v. 43, p. 2–32, https://doi.org/10.1016/j.jsg.2012.05.004.

Handin, J., 1966, Strength and ductility, *in* Clark, S.P., Jr., ed., Handbook of Physical Constants: Geological Society of America Memoir 97, p. 223–290, https://doi.org/10.1130/MEM97-p223.

Hayman, N.W., 2006, Shallow crustal fault rocks from the Black Mountains detachments, Death Valley, CA: Journal of Structural Geology, v. 28, p. 1767–1784, https://doi.org/10.1016/j.jsg.2006.06.017.

Howard, K.A., and John, B.E., 1987, Crustal extension along a rooted system of low-angle faults: Colorado River extensional corridor, California and Arizona, *in* Coward, M.P, Dewey, J.F., and Hancock, P.L., eds., Continental Extensional Tectonics: Geological Society [London] Special Publication 28, p. 299–311, https://doi.org/10.1144/GSL.SP.1987.028.01.19.

Jackson, J.A., and White, N.J., 1989, Normal faulting in the upper continental crust: Observations from regions of active extension: Journal of Structural Geology, v. 11, p. 15–36, https://doi.org/10.1016/0191-8141(89)90033-3.

Jacobson, C.E., Grove, M., Stamp, M.M., Vucic, A., Oyarzabal, F.R., Haxel, G.B., Tosdal, R.M., and Sherrod, D.R., 2002, Exhumation history of the Orocopia Schist and related rocks in the Gavilan Hills area of southeasternmost California, *in* Barth, A., ed., Contributions to Crustal Evolution of the Southwestern United States: Geological Society of America Special Paper 365, p. 129–154.

Jacobson, C.E., Grove, M., Vucic, A., Pedrick, J.N., and Ebert, K.A., 2007, Exhumation of the Orocopia Schist and associated rocks of southeastern California: Relative roles of erosion, synsubduction tectonic denudation and middle Cenozoic extension, *in* Cloos, M., ed., Convergent Margin Terranes and Associated Regions: A Tribute to W.G. Ernst: Geological Society of America Special Paper 419, p. 1–37, https://doi.org/10.1130/2007.2419(01).

Karner, S.L., Marone, C., and Evans, B., 1997, Laboratory study of fault healing and lithification in simulated fault gouge under hydrothermal conditions: Tectonophysics, v. 277, p. 41–55, https://doi.org/10.1016/S0040-1951(97)00077-2.

Karson, J.A., Früh-Green, G.L., Kelley, D.S., Williams, E.A., Yoerger, D.R., and Jakuba, M., 2006, Detachment shear zone of the Atlantis Massif core complex, Mid-Atlantic Ridge, 30°N: Geochemistry Geophysics Geosystems, v. 7, Q06016, https://doi.org/10.1029/2005GC001109.

Kumar, P., and Kawakatsu, H., 2011, Imaging the seismic lithosphere-asthenosphere boundary of the oceanic plate: Geochemistry Geophysics Geosystems, v. 12, Q01006, https://doi.org/10.1029/2010GC003358.

Lavier, L.L., Buck, W.R., and Poliakov, A.N.B., 1999, Self-consistent rolling-hinge model for the evolution of large-offset, low-angle normal faults: Geology, v. 27, p. 1127–1130, https://doi.org/10.1130/0091-7613(1999)027<1127:SCRHMF>2.3.CO;2.

Lee, C.-T., Qingzhu, Y., Rudnick, R.L., and Jacobsen, S.B., 2001, Preservation of ancient and fertile lithospheric mantle beneath the southwestern United States: Nature, v. 411, p. 69–73, https://doi.org/10.1038/35075048.

Lister, G.S., and Davis, G.A., 1989, The origin of metamorphic core complexes and detachment faults formed during Tertiary continental extension in the northern Colorado River region, U.S.: Journal of Structural Geology, v. 11, p. 65–94, https://doi.org/10.1016/0191-8141(89)90036-9.

Lister, G.S., Banga, G., and Feenstra, A., 1984, Metamorphic core complexes of Cordilleran type in the Cyclades, Aegean Sea, Greece: Geology, v. 12, p. 221–225, https://doi.org/10.1130/0091-7613(1984)12<221:MCCOCT>2.0.CO;2.

Little, T.A., Webber, S.M., Mizera, M., Boulton, C., Oesterle, J., Ellis, S., Boles, A., van der Pluijm, B., Norton, K., Seward, D., Biemiller, J., and Wallace, L., 2019, Evolution of a rapidly slipping low-angle normal fault, Suckling-Dayman metamorphic core complex, SE Papua New Guinea: Geological Society of America Bulletin, v. 131, p. 1333–1363, https://doi.org/10.1130/B35051.1.

Liu, L., Gurnis, M., Seton, M., Saleeby, J., Müller, R.D., and Jackson, J.M., 2010, The role of oceanic plateau subduction in the Laramide orogeny: Nature Geoscience, v. 3, p. 353–357, https://doi.org/10.1038/ngeo829.

Lockner, D.A., Byerlee, J.D., Kuksenko, V., Ponomarev, A., and Sidorin, A., 1991, Quasi-static fault growth and shear fracture energy in granite: Nature, v. 350, p. 39–42, https://doi.org/10.1038/350039a0.

Logan, J.M., Dengo, C.A., Higgs, N.G., and Wang, Z.Z., 1992, Fabrics of experimental fault zones: Their development and relationship to mechanical behavior, *in* Evans, B., and Wong, T.-F., eds., Fault Mechanics and Transport Properties of Rocks: New York, Academic Press, p. 33–67, https://doi.org/10.1016/S0074-6142(08)62814-4.

Luffi, P., Saleeby, J.B., Lee, C.-T.A., and Ducea, M.N., 2009, Lithospheric mantle duplex beneath the central Mojave Desert revealed by xenoliths from Dish Hill, California: Journal of Geophysical Research, v. 114, B03202, https://doi.org/10.1029/2008JB005906.

Luther, A., Axen, G.J., and Selverstone, J., 2013, Particle-size distributions of low-angle normal fault breccias: Implications for slip mechanisms on weak faults: Journal of Structural Geology, v. 55, p. 50–61, https://doi.org/10.1016/j.jsg.2013.07.009.

Mandl, G., de Jong, L.N.J., and Maltha, A., 1977, Shear zones in granular materials: Rock Mechanics, v. 9, p. 95–144, https://doi.org/10.1007/BF01237876.

Marone, C., 1995, Fault zone strength and failure criteria: Geophysical Research Letters, v. 22, p. 723–726, https://doi.org/10.1029/95GL00268.

Martel, S.J., and Pollard, D.D., 1989, Mechanics of slip and fracture along small faults and simple strike-slip fault zones in granitic rock: Journal of Geophysical Research, v. 94, p. 9417–9428, https://doi.org/10.1029/JB094iB07p09417.

McQuarrie, N., and Oskin, M., 2010, Palinspastic restoration of NAVDat and implications for the origin of magmatism in southwestern North America: Journal of Geophysical Research, v. 115, B10410, https://doi.org/10.1029/2009JB006435.

Miller, E.L., Gans, P.B., and Garing, J., 1983, The Snake Range décollement: An exhumed mid-Tertiary brittle-ductile transition: Tectonics, v. 2, p. 239–263, https://doi.org/10.1029/TC002i003p00239.

Mitchell, T.M., Toy, V., Di Toro, G., Renner, J., and Sibson, R.H., 2016, Fault welding by pseudotachylyte formation: Geology, v. 44, p. 1059–1062, https://doi.org/10.1130/G38373.1.

Nicholson, C., Sorlien, C.C., Atwater, T., Crowell, J.C., and Luyendyk, B.P., 1994, Microplate capture, rotation of the western Transverse Ranges, and initiation of the San Andreas transform as a low-angle fault system: Geology, v. 22, p. 491–495, https://doi.org/10.1130/0091-7613(1994)022<0491:MCROTW>2.3.CO;2.

Niu, Y., and Batiza, R., 1991, In situ densities of MORB melts and residual mantle: Implications for buoyancy forces beneath mid-ocean ridges: The Journal of Geology, v. 99, p. 767–775, https://doi.org/10.1086/629538.

Ortega-Arroyo, D., Behr, W.M., and Gentry, E., 2017, The rock record of seismic nucleation: Examples from pseudotachylites beneath the Whipple detachment fault, eastern California: New Orleans, Louisiana, American Geophysical Union, Fall Meeting 2017, abstract MR43D-0499.

Proctor, B., and Lockner, D.A., 2016, Pseudotachylyte increases the post-slip strength of faults: Geology, v. 44, p. 1003–1006, https://doi.org/10.1130/G38349.1.

Reston, T.J., 2009, The structure, evolution and symmetry of the magma-poor rifted margins of the North and Central Atlantic: A synthesis: Tectonophysics, v. 468, p. 6–27, https://doi.org/10.1016/j.tecto.2008.09.002.

Saleeby, J., 2003, Segmentation of the Laramide slab—Evidence from the southern Sierra Nevada region: Geological Society of America Bulletin, v. 115, p. 655–668, https://doi.org/10.1130/0016-7606(2003)115<0655:SOTLSF>2.0.CO;2.

Selverstone, J., Axen, G.J., and Luther, A., 2012, Fault localization controlled by fluid infiltration into mylonites: Formation and strength of low-angle normal faults in the midcrustal brittle-plastic transition: Journal of Geophysical Research, v. 117, B06210, https://doi.org/10.1029/2012JB009171.

Severinghaus, J., and Atwater, T., 1990, Cenozoic geometry and thermal state of the subducting slabs beneath western North America, *in* Wernicke, B.P., ed., Basin and Range Extensional Tectonics at the Latitude of Las Vegas, Nevada: Geological Society of America Memoir 176, p. 1–22, https://doi.org/10.1130/MEM176-p1.

Sibson, R.H., 1985, A note on fault reactivation: Journal of Structural Geology, v. 7, p. 751–754, https://doi.org/10.1016/0191-8141(85)90150-6.

Singleton, J.S., and Mosher, S., 2012, Mylonitization in the lower plate of the Buckskin-Rawhide detachment fault, west-central Arizona: Implications for the geometric evolution of metamorphic core complexes: Journal of Structural Geology, v. 39, p. 180–198, https://doi.org/10.1016/j.jsg.2012.02.013.

Singleton, J.S., Stockli, D.F., Gans, P.B., and Prior, M.G., 2014, Timing, rate, and magnitude of slip on the Buckskin-Rawhide detachment fault, west central Arizona: Tectonics, v. 33, p. 1596–1615, https://doi.org/10.1002/2013TC003517.

Smith, S.A.F., Collettini, C., and Holdsworth, R.E., 2008, Recognizing the seismic cycle along ancient faults: CO_2-induced fluidization of breccias in the footwall of a sealing low-angle normal fault: Journal of Structural Geology, v. 30, p. 1034–1046, https://doi.org/10.1016/j.jsg.2008.04.010.

Smithson, S.B., 1971, Densities of metamorphic rocks: Geophysics, v. 36, p. 690–694, https://doi.org/10.1190/1.1440205.

Spencer, J.E., 1984, Role of tectonic denudation in warping and uplift of low-angle normal faults: Geology, v. 12, p. 95–98, https://doi.org/10.1130/0091-7613(1984)12<95:ROTDIW>2.0.CO;2.

Spencer, J.E., and Chase, C.G., 1989, Role of crustal flexure in initiation of low-angle normal faults and implications for structural evolution of the Basin and Range Province: Journal of Geophysical Research, v. 94, p. 1765–1775, https://doi.org/10.1029/JB094iB02p01765.

Spencer, J.E., and Reynolds, S.J., 1989, Middle Tertiary tectonics of Arizona and adjacent areas, *in* Jenney, J.P., and Reynolds, S.J., eds., Geological Evolution of Arizona: Arizona Geological Society Digest 17, p. 539–574.

Spencer, J.E., and Reynolds, S.J., 1991, Tectonics and mid-Tertiary extension along a transect through west-central Arizona: Tectonics, v. 10, p. 1204–1221, https://doi.org/10.1029/91TC01160.

Strickland, E.D., Singleton, J.S., and Haxel, G.B., 2018, Orocopia Schist in the northern Plomosa Mountains, west-central Arizona: A Laramide subduction complex exhumed in a Miocene metamorphic core complex: Lithosphere, v. 10, p. 723–742, https://doi.org/10.1130/L742.1.

Tsutsumi, A., and Shimamoto, T., 1997, High velocity frictional properties of gabbro: Geophysical Research Letters, v. 24, p. 699–702, https://doi.org/10.1029/97GL00503.

Wang, C.-Y., Okaya, D.A., Ruppert, C., Davis, G.A., Guo, T.-S., Zhong, Z., and Wenk, H.-R., 1989, Seismic reflectivity of the Whipple Mountain shear zone in southern California: Journal of Geophysical Research, v. 94, p. 2989–3005, https://doi.org/10.1029/JB094iB03p02989.

Wawrzyniec, T., Selverstone, J., and Axen, G.J., 1999, Correlations between fluid composition and deep-seated structural style in the footwall of the Simplon low-angle normal fault, Switzerland: Geology, v. 27, p. 715–718, https://doi.org/10.1130/0091-7613(1999)027<0715:CBFCAD>2.3.CO;2.

Wdowinski, S., and Axen, G.J., 1992, Isostatic rebound due to tectonic denudation: A viscous flow model of a layered lithosphere: Tectonics, v. 11, p. 303–315, https://doi.org/10.1029/91TC02341.

Wernicke, B., 1981, Low-angle normal faults in the Basin and Range Province: Nappe tectonics in an extending orogen: Nature, v. 291, p. 645–648, https://doi.org/10.1038/291645a0.

Wernicke, B., 1995, Low-angle normal faults and seismicity: A review: Journal of Geophysical Research, v. 100, p. 20159–20174, https://doi.org/10.1029/95JB01911.

Wernicke, B., and Axen, G.J., 1988, On the role of isostasy in the evolution of normal faults: Geology, v. 16, p. 848–851, https://doi.org/10.1130/0091-7613(1988)016<0848:OTROII>2.3.CO;2.

Wernicke, B., and Burchfiel, B.C., 1982, Modes of extensional tectonics: Journal of Structural Geology, v. 4, p. 105–115, https://doi.org/10.1016/0191-8141(82)90021-9.

Wernicke, B., Walker, J.D., and Beaufait, M.S., 1985, Structural discordance between Neogene detachments and frontal Sevier thrusts, central Mormon Mountains, southern Nevada: Tectonics, v. 4, p. 213–246, https://doi.org/10.1029/TC004i002p00213.

Westaway, R., 1999, The mechanical feasibility of low-angle normal faulting: Tectonophysics, v. 308, p. 407–443, https://doi.org/10.1016/S0040-1951(99)00148-1.

Whitney, D.L., and Dilek, Y., 1997, Core complex development in central Anatolia, Turkey: Geology, v. 25, p. 1023–1026, https://doi.org/10.1130/0091-7613(1997)025<1023:CCDICA>2.3.CO;2.

Whitney, D.L., Teyssier, C., Rey, P., and Buck, W.R., 2013, Continental and oceanic core complexes: Geological Society of America Bulletin, v. 125, p. 273–298, https://doi.org/10.1130/B30754.1.

Wust, S.L., 1986, Regional correlation of extension directions in Cordilleran metamorphic core complexes: Geology, v. 14, p. 828–830, https://doi.org/10.1130/0091-7613(1986)14<828:RCOEDI>2.0.CO;2.

Yin, A., 1989, Origin of regional, rooted low-angle normal faults: A mechanical model and its tectonic implications: Tectonics, v. 8, p. 469–482, https://doi.org/10.1029/TC008i003p00469.

Yin, A., and Dunn, J.F., 1992, Structural and stratigraphic development of the Whipple-Chemehuevi detachment fault system, southeastern California: Implications for the geometrical evolution of domal and basinal low-angle normal faults: Geological Society of America Bulletin, v. 104, p. 659–674, https://doi.org/10.1130/0016-7606(1992)104<0659:SASDOT>2.3.CO;2.

Yuan, X.P., Christie-Blick, N., and Braun, J., 2017, Mechanical properties of the Sevier Desert detachment: An application of critical Coulomb wedge theory: Geophysical Research Letters, v. 45, p. 7417–7424, https://doi.org/10.1029/2017GL076854.

Science Editor: Wenjiao Xiao
Associate Editor: Karel Schulmann

Manuscript Received 10 June 2019
Revised Manuscript Received 22 October 2019
Manuscript Accepted 18 November 2019

Printed in the USA